


## ORIGINAL ARTICLE

# Effects of intermediate energy heavy-ion irradiation on the microstructure of rutile TiO<sub>2</sub> single crystal

Kassiopeia A. Smith<sup>1</sup>  | Andreas I. Savva<sup>1</sup> | Yaqiao Wu<sup>1,2</sup> | Dmitri A. Tenne<sup>3</sup> | Darryl P. Butt<sup>4</sup> | Hui Xiong<sup>1</sup> | Janelle P. Wharry<sup>5</sup>

<sup>1</sup>Micron School of Materials Science & Engineering, Boise State University, Boise, Idaho

<sup>2</sup>Center for Advanced Energy Studies, 995 University Boulevard, Idaho Falls, Idaho

<sup>3</sup>Department of Physics, Boise State University, Boise, Idaho

<sup>4</sup>College of Mines and Earth Sciences, University of Utah, Salt Lake City, Utah

<sup>5</sup>School of Nuclear Engineering, Purdue University, West Lafayette, Indiana

## Correspondence

Hui (Claire) Xiong, Micron School of Materials Science & Engineering, Boise State University, Boise, ID.

Email: [clairexiong@boisestate.edu](mailto:clairexiong@boisestate.edu) and

Janelle P. Wharry, School of Nuclear Engineering, Purdue University, West Lafayette, IN.

Email: [jwharry@purdue.edu](mailto:jwharry@purdue.edu)

## Funding information

National Science Foundation, Grant/Award

Number: DMR-1408949; Nuclear

Regulatory Commission, Grant/Award

Number: NRC-HQ-84-14-G-0056

## Abstract

This study reports the microstructure evolution of single crystal rutile TiO<sub>2</sub> under 3 MeV Nb<sup>+</sup> ion irradiation, with the irradiating ions incident on the {100} plane. A complex, multi-layered microstructure evolution is observed with 4 distinct regions: (i) short-range disorder in the first 60 nm below the specimen surface, (ii) dislocation loops oriented parallel to the incident ion beam direction, located along the increasing slope of the irradiation damage profile at ~60-650 nm from the surface, (iii) loops oriented perpendicular to the incident ion beam direction, at depths encompassing the ion implantation and irradiation damage peaks ~650-1250 nm, and (iv) a high density of nano-scale atomic rearrangements with long-range order, located at depths ~1250-1750 nm. These results present evidence that multiple defect mechanisms occur during irradiation including ion channeling, nuclear stopping, and electronic stopping interactions as a function of depth and disorder accumulation.

## KEYWORDS

dislocation loops, high-resolution transmission electron microscope, ion irradiation, titanium dioxide

## 1 | INTRODUCTION

Titanium dioxide (TiO<sub>2</sub>) is an important material used across many scientific and industrial sectors with applications ranging from cosmetics and plastics to water purification and energy storage.<sup>1-3</sup> TiO<sub>2</sub> is widely regarded as an ideal functional material because of its low cost, high chemical stability, and safety in terms of both human and environmental impact. TiO<sub>2</sub> is also an important material for a variety of sensor, optoelectrical, nuclear waste, and absorption applications, during which the material will be exposed to irradiation. Hence, the effects of irradiation on

the TiO<sub>2</sub> must be understood. In recent years, a body of work has been generated on the effects of irradiation on TiO<sub>2</sub>.<sup>4-34</sup>

Separate studies by Zheng et al and Qin et al indicated that photovoltaic properties were increased in thin film anatase substrates when irradiated with low-energy metal ions to nominal doses (10<sup>13</sup> to 10<sup>16</sup> ions cm<sup>-2</sup>),<sup>14,20</sup> though Zheng et al later argued that higher doses (10<sup>17</sup> ions cm<sup>-2</sup>) caused recombination centers to form resulting in reduced overall photocatalytic activity.<sup>13</sup> In addition to photocatalytic applications, Jensen et al observed that irradiating with Fe ions at doses of 10<sup>16</sup> ions cm<sup>-2</sup> induced

ferromagnetic behavior.<sup>25</sup> Other studies have shown enhancement of UV and optical absorption, and water splitting behaviors in anatase thin films with similar irradiation conditions.<sup>15,24</sup> In studying rutile thin films, it has been observed that rutile has better resistance to amorphization than other TiO<sub>2</sub> polymorphs, possibly due to atomic packing densities.<sup>15,18,22</sup> Computational simulations by Uberuagaa, Qin, and Lumpkin have supported these experiments and given details into the mechanisms of defect accumulation and amorphization resistance.<sup>12,19,22</sup> Temperature dependence studies by Li et al have shown that when irradiating at higher temperatures, point defects were more mobile and allowed for damage recovery. Conversely, at room temperature the irradiation damage was more likely to form stable irradiation-induced point defects<sup>30</sup> which was later supported by Zhang and coworkers.<sup>28</sup> Hartmann et al showed that using lighter irradiation species such as He<sup>+</sup> are more likely to amorphize target substrates than heavy noble gases such as Xe<sup>2+</sup> and Ne<sup>+</sup>.<sup>33</sup> Our recent study showed that proton irradiation could induce phase transformation in amorphous TiO<sub>2</sub> nanotubes to a disordered rutile phase at temperature of 250°C.<sup>34</sup>

Although these recent studies have shed light on the effects of irradiation on the order and functionality of TiO<sub>2</sub>, there remains limited understanding of the underlying microstructure-based mechanisms for these irradiation-induced changes. Fundamental microstructural phenomena are difficult to ascertain because many of these aforementioned irradiation studies of TiO<sub>2</sub> have utilized low-energy implantations (i.e., tens to a few hundred keV) on polycrystalline substrates. The shallow damage profiles from ~keV irradiation renders it difficult to resolve differences in microstructure evolution as a function of depth, a task which is further complicated by the presence of interfaces and grain boundaries in polycrystalline materials. Basic irradiation-induced microstructure evolution mechanisms may be more readily observed if a single crystal specimen is irradiated with intermediate-energy heavy ions. Nb<sup>+</sup> ions have been chosen in this case, as niobium doping has widely been used to enhance a variety of properties of TiO<sub>2</sub>.<sup>35–42</sup>

The objective of this study is to examine the defect microstructures, which arise from Nb<sup>+</sup> ion irradiation on the {100} orientation of rutile single crystal TiO<sub>2</sub>. Though rutile is thought to be more resistant to irradiation-induced amorphization, it is selected for this study because the mechanism for atomic rearrangement and the resulting disordered crystalline matrix is not yet known. Microstructure characterization utilizes a combination of X-ray diffraction, Raman spectroscopy, and transmission electron microscopy. Results from each technique will be presented individually and then integrated to understand the complex layered microstructure evolution.

## 2 | METHODS

### 2.1 | Materials and irradiation

Rutile single crystal TiO<sub>2</sub> (100) specimens, 5 × 5 × 0.5 mm, were obtained from MTI Corp. for ion irradiation. The surface finish was <5 Å to reduce the amount of surface residual stress and damage, to which the near-surface ion irradiation damage layer is sensitive. Specimens were oriented such that the (100) plane was perpendicular to the ion beam. Irradiation with 3 MeV Nb<sup>+</sup> ions was conducted using a raster-scanned beam at high vacuum (<10<sup>-7</sup> torr) in the 1.7 MV General Ionex Tandetron at the Michigan Ion Beam Laboratory with an average current of 52.8 nA, and a fluence of 4.03 × 10<sup>11</sup> ions/s over a 0.4 cm<sup>2</sup>, which translates to a dose rate of 9.28 × 10<sup>-4</sup> dpa/s. Raster scanning occurred at a frequency of 2061 Hz in the vertical direction and 255 Hz in the horizontal direction. The duration of one scanning cycle was 0.48 ms in the vertical and 3.92 ms in the horizontal. The ratio of the vertical to horizontal scanning cycles was a noninteger number, such that the beam path was offset from the previous scan cycle, ensuring good spatial uniformity of the scanned beam area. Because the beam scanning occurred at such a rapid frequency, and because the beam cycle fully and uniformly covered the specimen, the thermal effect on the specimen was uniform (i.e., nonlocalized) heating. We utilized a thermal imaging system to initially calibrate the specimen to the desired room temperature and then monitored the specimen temperature continually throughout the experiment. The thermal imaging system had temperature resolution ±2°C and spatial resolution 5–14 μm (depending on the distance between the specimen and the thermal imaging system's focal plane). This spatial resolution was significantly lower than the 3 mm diameter of the rastered beam and thus would be sufficient to detect local heating from the beam. During irradiation, the specimen back temperature was maintained using a combination of a liquid nitrogen cooling loop and a cartridge heater. This combined heating and cooling approach enabled higher precision control of the specimen temperature. Temperatures recorded throughout the experiment show that all regions of the specimen never exceeded more than 20°C above room temperature.

The irradiation damage profile (Figure 1) was calculated from the “Quick Calculation” or Kinchin-Pease mode<sup>43</sup> within Stopping Range of Ions in Matter (SRIM) 2013<sup>44</sup>; displacements were obtained from the vacancy.txt file. SRIM calculations used a 0.5 mm compact layer of TiO<sub>2</sub>, with a density of 4.23 g/cm<sup>3</sup>, and displacement energies of 25 and 28 eV for Ti and O, respectively. The damage profile corresponded to a dose of 6.5 displacements per atom (dpa) at the sample surface, rising to 23 dpa at the damage

peak, which was located  $\sim 900$  nm from the surface. The  $\text{Nb}^+$  implantation peak was located approximately 1100 nm below the sample surface with a maximum implantation depth of  $\sim 1.45$   $\mu\text{m}$ .

## 2.2 | Microscopy

Site-specific transmission electron microscopic (TEM) lamella lift-out specimens were made using the FEI Quanta 3D FEG FIB at the Microscopy and Characterization Suite (MaCS) Center for Advanced Energy Studies (CAES).<sup>45</sup> Prior to milling, a layer of platinum was deposited to protect the original irradiated surface. The TEM lamellae were bulk milled at 30 kV to form a rectangular cross section that was approximately  $15\ \mu\text{m} \times 10\ \mu\text{m} \times 100$  nm, followed by further milling at 5 kV to a thickness of about 50-100 nm. Last, a 2 kV cleaning step was applied to reduce surface damage incurred on the surface of the sample by the milling steps. Two sets of TEM lamellae were made in order to observe the microstructure in 2 directions: the first set was oriented perpendicular to the irradiated surface (i.e., parallel to the ion beam direction), such that the ion irradiation damage profile was observed through the depth of the specimen, while the second set was perpendicular to the ion beam direction.

Transmission electron microscopic specimens were analyzed using an FEI Tecnai TF30-FEG STwin STEM at CAES, which had a point-to-point resolution of 0.19 nm in TEM mode. In order to characterize the mesoscopic irradiated microstructure, specimens were tilted to the pole axis and observed in bright field imaging mode.<sup>46</sup> High-resolution-TEM (HR-TEM) imaging was subsequently utilized to ascertain information about crystallinity.

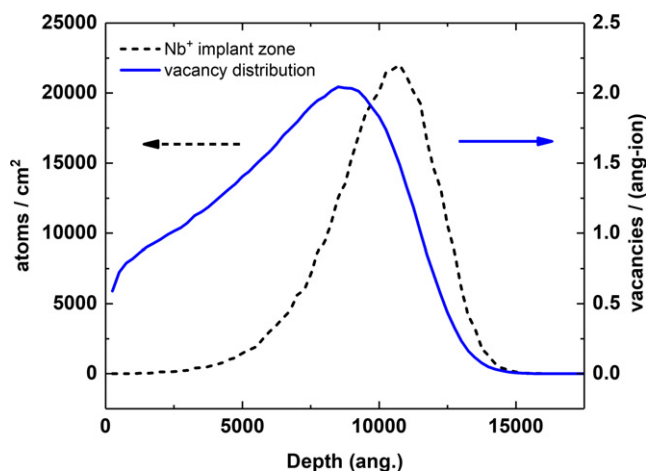


**FIGURE 1** SRIM calculation of implanted  $\text{Nb}^+$  ions (dashed line, left axis) and the resulting irradiation damage profile (solid line, right axis) for rutile  $\text{TiO}_2$ . SRIM, Stopping Range of Ions in Matter

## 2.3 | Raman spectroscopy and X-ray diffraction

The single crystal samples were evaluated using Raman spectroscopy and X-ray diffraction (XRD). Raman has long been used to characterize the local and long-range order of crystalline samples by giving insight to dynamic interactions of the lattice structure, and has been widely used to investigate the various polymorphs of  $\text{TiO}_2$ . Hence, there is a wide body of literature on the Raman response of this material.<sup>47–53</sup> XRD is a complimentary technique, which provides information on the overall crystallinity and phase of the material.<sup>54</sup>

Raman spectra were measured in backscattering geometry using a Jobin Yvon T64000 triple spectrometer equipped with a liquid nitrogen cooled multichannel charge coupled device detector. The 325 nm line of He-Cd laser and 514.5 nm line of Ar ion lasers were used for excitation; maximum laser power density is  $0.5\ \text{W}/\text{mm}^2$  at the sample surface. Spectra are recorded at 10 K using an evacuated closed cycle helium cryostat. XRD was obtained by Rigaku Miniflex diffractometer with  $\text{Cu K}_\alpha$  irradiation at  $\lambda = 1.5406\ \text{\AA}$ .

## 3 | RESULTS AND DISCUSSION

$\text{TiO}_2$  is a wide band-gap material and absorbs light in the ultraviolet (UV) region. The Nb-ion irradiated rutile  $\text{TiO}_2$  (100) samples evolved from transparent to an opaque black color, which was indicative of defect production that altered the band structure of  $\text{TiO}_2$ . The irradiation-induced structural and microstructural changes were studied using TEM, Raman, and XRD.

### 3.1 | Structural characterization

Rutile is the most thermodynamically stable form of  $\text{TiO}_2$  with a tetragonal  $\text{P4}_2/\text{mnm}$  space-group, where  $a = b = 4.625\ \text{\AA}$  and  $c = 2.959\ \text{\AA}$ . The unit cell is comprised of 2  $\text{TiO}_2$  molecules with each Ti atom having 6 oxygen nearest neighbors. The 4 Raman active vibrational modes found in rutile  $\text{TiO}_2$  are  $\text{B}_{1g}$  ( $143\ \text{cm}^{-1}$ ),  $\text{E}_g$  ( $447\ \text{cm}^{-1}$ ),  $\text{A}_{1g}$  ( $612\ \text{cm}^{-1}$ ), and  $\text{B}_{2g}$  ( $826\ \text{cm}^{-1}$ ).<sup>52,55</sup> Raman spectroscopy can be conducted at a range of energies by altering the laser excitation wavelength, which in turn affects which vibrational modes are activated, in addition to the depth of the investigation.

Raman spectra were first obtained using a UV laser (325 nm wavelength), which sampled the top 5-10 nm of the specimen.<sup>50</sup> In this region (Figure 2A), both the unirradiated and  $\text{Nb}^+$  irradiated samples exhibited a broad band near  $213\ \text{cm}^{-1}$ , which was attributed to a combinatorial

band,<sup>52</sup> as well as a sharp peak at  $612\text{ cm}^{-1}$  corresponding to the  $A_{1g}$  band. These 2 bands were largely unaltered by the irradiation. On the other hand, in the  $\text{Nb}^+$  irradiated sample, a sharp  $B_{2g}$  peak emerged at  $826\text{ cm}^{-1}$ . This band is not commonly observed in  $\text{TiO}_2$ , and when it does appear, it is typically a weak signal<sup>56</sup> unlike the clearly defined peak shown herein. The  $B_{2g}$  vibrational mode represents an antisymmetric Ti–O distortion of the  $\text{TiO}_6$  octahedra, which is sensitive to the local environment of the Ti ions.<sup>56,57</sup> This marked increase in the  $B_{2g}$  mode suggests that the local Ti environment changed, leading to an increase in the vibrational intensity of this mode.

Raman spectra were also obtained using an argon laser ( $514.4\text{ nm}$  wavelength), which sampled depths of approximately  $1\text{ }\mu\text{m}$  for  $\text{TiO}_2$ .<sup>50</sup> There was no significant difference between the Raman spectra of the unirradiated and irradiated samples at this wavelength (Figure 2B). Results from both excitation wavelengths ( $325$  and  $514.4\text{ nm}$ ) collectively suggest that while the majority of the irradiated region appears to maintain long-range order, the surface  $5\text{--}10\text{ nm}$  region of the specimen has an altered binding state containing a higher concentration of defects.

The XRD spectrum (Figure 3) exhibited  $2\theta$  peaks at approximately  $39.3^\circ$  and  $84.3^\circ$ , which correspond to the 100 rutile structure. After  $\text{Nb}^+$  irradiation, these peaks shifted to smaller angles by  $\sim 0.1\text{--}0.2^\circ$ , suggesting that the irradiated rutile structure has larger unit cell. This finding corroborates the Raman results, which indicate disorder at the surface of the specimen. The irradiated rutile XRD spectrum also exhibited peak broadening and a reduction in

intensity, which can be attributed to the disorders induced by irradiation.

### 3.2 | Microstructural characterization

Transmission electron microscopic revealed microstructure evolution induced by  $\text{Nb}^+$  irradiation. Cross-sectional TEM lamellae were prepared from the ion-implanted crystals to examine the nature and distribution of defects as a function of depth along the damage profile. In-plane lamellae were also prepared to characterize the spatial extent of defects at depths of interest as determined by the results of imaging the cross-sectional lamellae. Results from both lamellae orientations are presented below.

The cross-sectional TEM lamella revealed 4 distinct damage regions (Figure 4), ranging from the surface to a depth of  $\sim 1700\text{ nm}$ . It is not unusual for irradiated rutile single crystals to exhibit different damage microstructures near the damage and implantation peaks, as compared with the near-surface region.<sup>58–61</sup> However, none of these previous studies reported such a complex, multi-layered defect structure as that observed herein. The multi-layered damage structure could be associated with the energy of the irradiation ion, which is an order of magnitude larger than those reported.<sup>58–61</sup> Characteristics of each of these 4 layers are described below in greater detail.

#### 3.2.1 | Region 1

The damage region within  $60\text{ nm}$  of the initial irradiated surface, which corresponds to an irradiation dose of

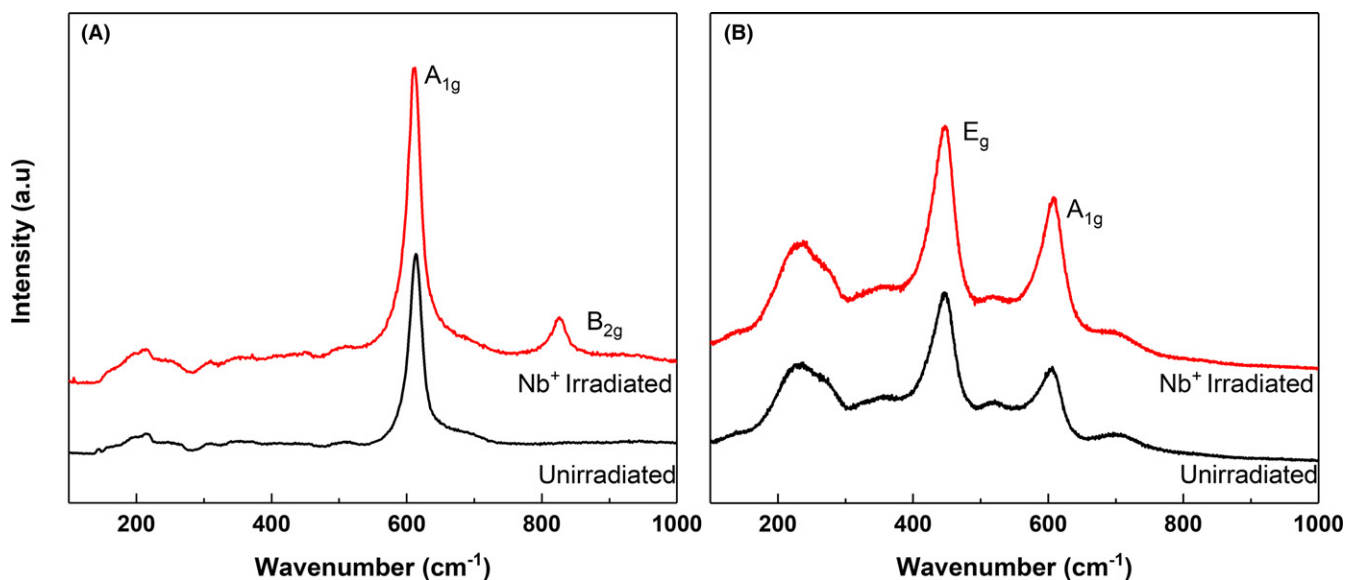


**FIGURE 2** Raman spectra of unirradiated rutile  $\text{TiO}_2$  single crystal (black), and niobium-irradiated rutile single crystal (red) using (A)  $325\text{ nm}$  laser wavelength with  $\sim 10\text{ nm}$  sampling depth and (B)  $514.5\text{ nm}$  wavelength laser with  $\sim 1000\text{ nm}$  sampling depth



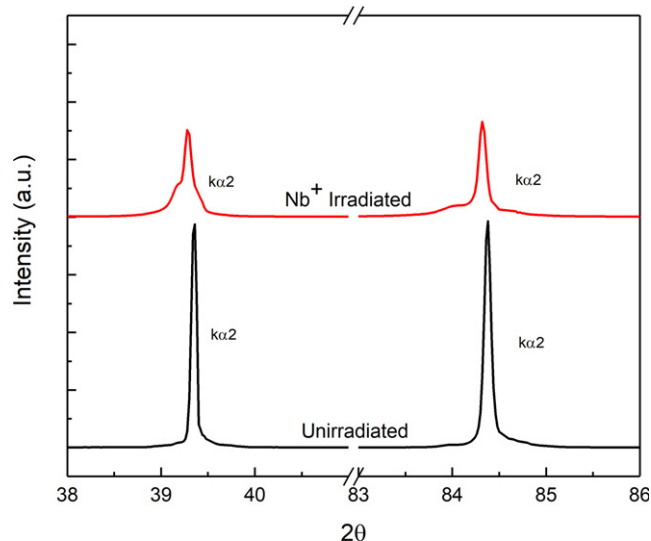


**FIGURE 3** XRD spectra of unirradiated rutile single crystal  $\text{TiO}_2$  (black) and  $\text{Nb}^+$  irradiated single crystal  $\text{TiO}_2$  (red)

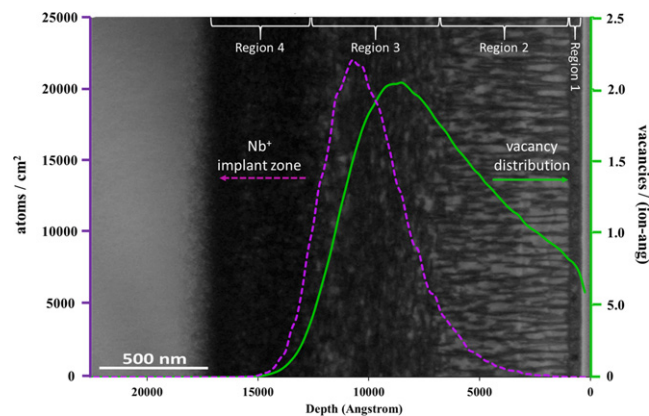


**FIGURE 4** Cross-sectional TEM micrograph of 4 distinct damage regions created in rutile single crystal  $\text{TiO}_2$ , with SRIM calculated damage profile (solid) and  $\text{Nb}^+$  implantation profile (dashed) overlaid. TEM, transmission electron microscope

~9 dpa, exhibits a homogeneous bright field (BF) contrast. From the HR-TEM imaging of this region (Figure 5A, B), we see that within the first 10 nm of Region 1 the sample is heavily disordered and the corresponding convergent beam electron diffraction (CBED) of the region indicates reorientation into the 101 direction (Figure 5C). Since this region is only about 60 nm, CBED technique is selected rather than general selected area electron diffraction (SAED) technique. This result is consistent with an earlier report from Li et al, in which rutile 100 single crystals were irradiated with 360 KeV  $\text{Xe}^{2+}$  ions, and the 12 nm region nearest to the surface was reoriented into the 011 orientation.<sup>60</sup> This finding is in agreement with our UV Raman result, which shows

short-range disorder of the surface region while maintaining long-range order.

### 3.2.2 | Region 2

This 650 nm region contains defects, potentially ion tracks or dislocation loops, that tend to be aligned parallel to the ion beam direction (Figure 6A, B). However, it has been reported that ion tracks only form in rutile  $\text{TiO}_2$  under swift heavy ion irradiation when electronic stopping exceeds 6.2 keV/nm.<sup>62,63</sup> Since the 2.5 MeV  $\text{Nb}^+$  ions herein do not provide sufficient electronic stopping, amorphous ion tracks are not expected to form. In-plane TEM lamellae from this region clearly reveal a network of dislocations (Figure 6D-F), ranging from 125 to 582 nm in length with a nonuniform branching structure. The dislocation loops appear as dark contrasting regions and exhibit significant disorder, while the lighter surrounding material consists of highly-ordered<sup>60</sup> oriented rutile regions. The order-disorder morphology of the loops and their immediate surroundings suggests that the loop formation mechanisms may partly be associated with electronic energy losses.<sup>64</sup>

In-plane TEM characterization revealed that the shape of the pristine material between dislocations is amebic and  $\sim 12 \text{ nm} \pm 4 \text{ nm}$  in width, and are spaced 20-160 nm apart (Figure 6D). In Region 2, the dislocations tend to form perpendicular to the highly stable  $\{100\}$  plane. Incoming Nb ions create a knock-on effect in the direction of irradiation causing dislocations to form in their path along the  $\langle 010 \rangle$  direction. As Raman spectroscopy indicates, long-range order is maintained and so the  $\{100\}$  plane is unchanged with irradiation. Towards the peak of the SRIM calculated damage cascade, the microstructure transitions into Region 3.

### 3.2.3 | Region 3

Dislocation loops were observed in the same lace-like microstructure as in Region 2, but are instead oriented perpendicular to the ion beam direction, or along the  $\{100\}$  plane (viz.  $90^\circ$  change in orientation from the loops in Region 2). Region 3 overlaps with the SRIM-calculated Nb ion implantation peak and encompasses the irradiation damage peak. This peak dose is 23 dpa and is approximately a factor of 2 larger than the dose in Region 2, which can explain the increased density of dislocation loops in Region 3 as compared with that in Region 2. Because the implanted ions come to rest as interstitials, the material must accommodate the excess volume. It is therefore reasonable that interstitial agglomerations or loops would be oriented on the  $\{100\}$  habit plane, enabling accumulation of defects along the  $[100]$  direction.<sup>65</sup> This is

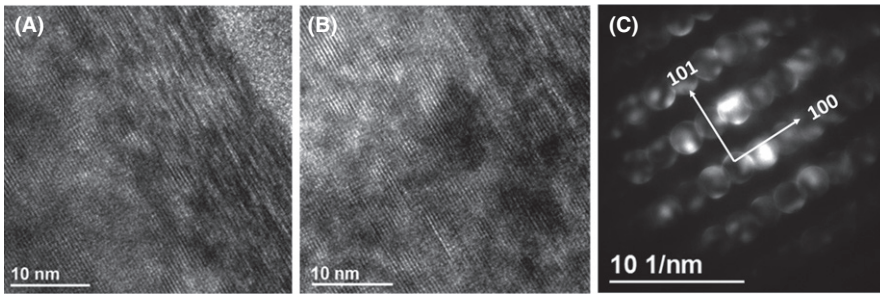


**FIGURE 5** HR-TEM (A) and (B) of the damage Region 1 in Nb<sup>+</sup> irradiated single crystal TiO<sub>2</sub>, and (C) corresponding CBED pattern

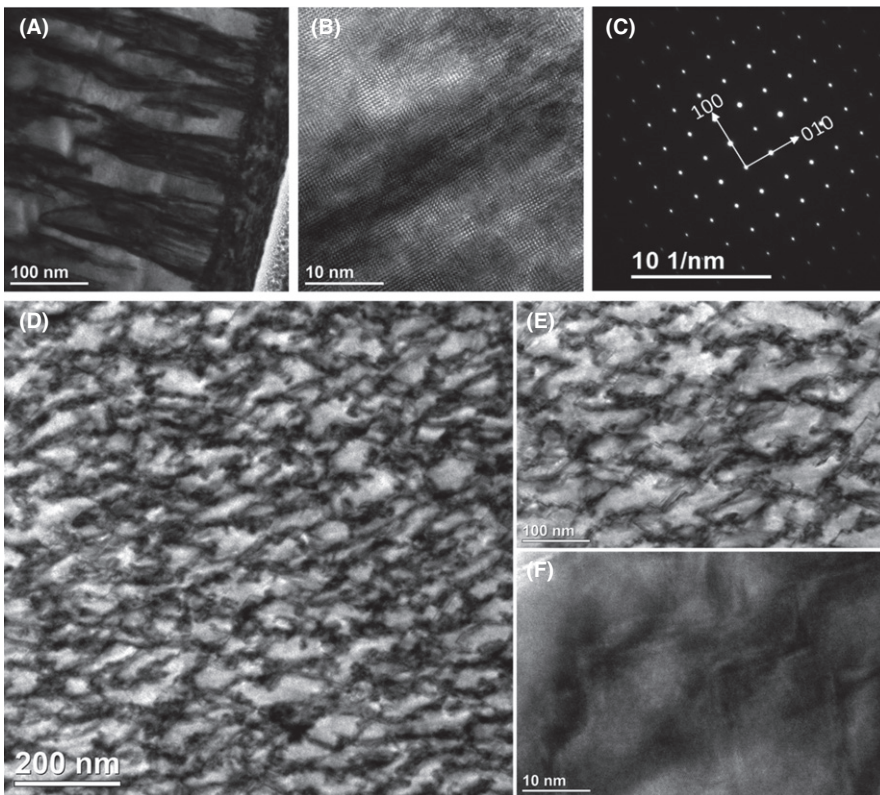


**FIGURE 6** (A) Bright field cross-sectional TEM of the transition between Region 1 and Region 2 of the irradiated single crystal, (B) HR-TEM showing dislocations parallel to the ion beam direction, and (C) corresponding SAED diffraction of Region 2. The in-plane TEM of Region 2 showing (D) low magnification and (E-F) high-resolution TEM images of the defect regions

because the atoms on the (100) plane tend to reconstruct when broken due to the high energy of the plane, causing the natural direction for growth and expansion in rutile TiO<sub>2</sub> to be in the [001] direction.

### 3.2.4 | Region 4

The final damage regime begins immediately beyond the Nb<sup>+</sup> implantation zone, then extends a further 500 nm into the substrate. The defects in this region are densely packed and comprised of nano-scale atomic rearrangements, maintaining the long-range crystalline ordering, as observed by SAED (Figure 7B). While the presence of defects deeper than the irradiation damage and implantation peaks may initially seem unusual, it is likely that ionic channeling is occurring as the ion beam is aligned with a major symmetry direction. While some of the incoming Nb<sup>+</sup> ions interact with the specimen as modeled, a percentage of the ions

do not come close enough to the atomic rows to cause scattering until farther along the ion trajectory. Similar results were shown by Weber et al when comparing channeling to nonchanneling orientations of SiC, whereas the channeling conditions experienced ionic penetration at much greater depths.<sup>66</sup>

### 3.3 | Energy deposition mechanisms through depth

The multi-layered defect structure, and the nature of these defects, can provide information about the unique energy loss mechanisms occurring at various depths.

Crystal reorientation in Region 1 may be attributed to ion channeling or one of several other mechanisms. Ion beam-induced or ion beam-assisted crystalline reorientation has been readily observed in a variety of materials, including transition-metal ceramics,<sup>67–69</sup> using ion beams as low

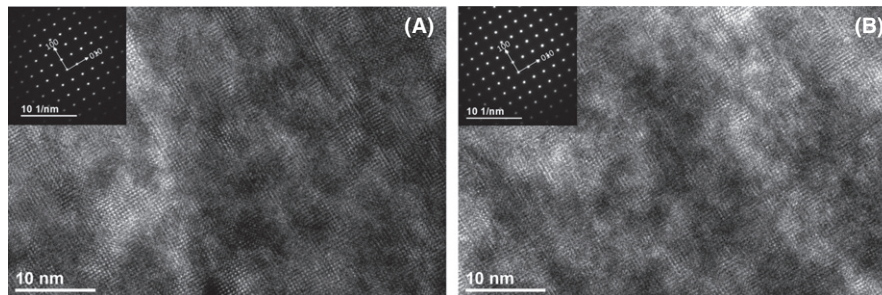


**FIGURE 7** HR-TEM and corresponding SAED patterns from (A) Region 3 and (B) Region 4 of the Nb<sup>+</sup> irradiated rutile single crystal TiO<sub>2</sub>

as a few hundred eV.<sup>69</sup> The reorientation can be understood to be driven by the ion channeling mechanism.<sup>69–73</sup> However, other mechanisms such as sputtering, surface energy, and deformation energy, are also plausible and all lead to the same reorientation as channeling.<sup>68</sup> The reorientation is also influenced by factors such as ion energy, defect population, and system temperature.<sup>73</sup> It has also been shown that bombardment with noble metal ions (e.g., Nb used in this study) induces more extensive reorientation in ceramics than does bombardment with noble gas ions.<sup>74</sup>

In Region 2, defect formation is an effect of irradiation damage. However, irradiation damage induced by “intermediate” energy ions (i.e., within the range ~0.5–5.0 MeV) is not well understood. The intermediate energy range has been most extensively studied by Backman and co-workers<sup>75,76</sup> for Au ions incident on silica (SiO<sub>2</sub>). Within this energy range, both nuclear and electronic stopping are important to the defect and microstructure evolution. Nuclear stopping is understood through binary collision approximation (BCA), while electronic stopping is understood through the inelastic thermal spike model.<sup>77,78</sup> The thermal spike model uses dense electronic excitations to transfer energy to the material through electron-phonon coupling, resulting in local heating along the ion trajectory (which often culminates in the formation of visible ion tracks). Backman’s results are noteworthy because they reveal that nuclear and electronic stopping exhibit a nonlinear synergy within the ion energy range of interest, resulting in a higher local defect density than would result from sequential evolution of atomic recoil processes and an inelastic thermal spike.<sup>75,76</sup> The synergistic effects of nuclear and electronic stopping have been described in the intermediate ion energy range in several ceramic systems.<sup>79–82</sup>

Although nuclear stopping is the dominant mechanism for defect creation for 3 MeV Nb ions, Backman’s work implies that electronic stopping processes can also contribute to damage creation. This is consistent with the order-disorder morphology of the loops and their local surroundings in Region 2—loops are created primarily by nuclear stopping event, but the disordering may partly be associated with inelastic thermal spike-type electronic stopping.<sup>64</sup>

Once the incident ion has lost its energy, it is likely that the microstructure evolution is influenced by the accumulation of defects in Region 3. As defects accumulate within Region 3, which corresponds to the peak of the calculated damage profile, the loop structures collapse along the (100) plane perpendicular to the ion beam. Because the ion fluence is not constant through the studied depth, it is worthwhile to consider the role of fluence on the microstructure evolution. Through Region 2, the fluence varies by approximately a factor of 2, with a higher fluence occurring deeper into the material. While this factor is not sufficient to induce an entirely different microstructure, it could potentially explain the appearance of a slightly higher density of defects deeper into Region 2 than at the shallower portion of Region 2. The fluence peaks within Region 3, which could explain the higher density of defects in Region 3 than in Region 2.

## 4 | CONCLUSIONS

We examined the microstructure evolution of single crystal rutile TiO<sub>2</sub> irradiated with 3 MeV Nb<sup>+</sup> ions, in which the ions are incident on the {100} plane. Characterization by TEM revealed a complex microstructure evolution, marked by 4 distinct layers or regions of damage. The TEM results, together with XRD and Raman spectroscopy, help to understand the four-region structure. The regions contain: (i) near-surface short-range disorder, (ii) dislocation loops parallel to the incident ion beam direction, (iii) loops perpendicular to the incident ion beam direction, and (iv) high-number density defects beyond the SRIM damage and implantation peaks.

The microstructures within each region are consistent with theories of varying irradiation damage mechanisms as a function of energy loss along the ion range. Ion-channeling-based damage is thought to account for crystallite reorientation and defect formation when the electronic stopping energy is high (i.e., near the surface of the specimen); this explains the formation of a high density of disorder in Region 1. When electronic stopping energy is lower, however (viz. deeper into the specimen), damage occurs primarily through nuclear stopping with a nonlinear



synergetic effect from electronic stopping inducing additional disorder. Near and beyond the ion implantation peak, buildup of defects cause collapse of the dislocation loops in Region 3, while ionic channeling can account for the accumulation of damage in Region 4, beyond the SRIM calculated damage profile.

## ACKNOWLEDGMENTS

The authors acknowledge support from the National Science Foundation under Grant No. DMR-1408949 and the Nuclear Regulatory Commission under Grant No. NRC-HQ-84-14-G-0056. The authors are also grateful to Dr. Ovidiu Toader and the staff members at the Michigan Ion Beam Laboratory for their assistance with ion irradiations, and to Dr. Karthik Chinnathambi for his assistance with indexing diffraction data.

## ORCID

Kassiopeia A. Smith  <http://orcid.org/0000-0003-4941-6587>

## REFERENCES

1. Bard AJ. Design of semiconductor photoelectrochemical systems for solar energy conversion. *J Phys Chem.* 1982;86:172-177.
2. Serpone N, Dondi D, Albini A. Inorganic and organic UV filters: their role and efficacy in sunscreens and sun care products. *Inorg Chim Acta.* 2007;360:794-802.
3. Rahimi N, Pax RA, Gray EM. Review of functional titanium oxides. I: TiO<sub>2</sub> and its modifications. *Prog Solid State Chem.* 2016;44:86-105.
4. Xu NN, Li GP, Lin QL, Liu H, Bao LM. Effect of Ar ion irradiation on the room temperature ferromagnetism of undoped and Cu-doped rutile TiO<sub>2</sub> single crystals. *Chin Phys B.* 2016;25:116103.
5. de Souza GB, Gonsalves SH, Ribeiro KC, Ditzel DG, Ueda M, Schreiner WH. Physical and chemical effects of the hydrogen irradiation on nitrided titanium surfaces. *Surf Coat Technol.* 2017;312:91-100.
6. Karlusic M, Jaksic M, Lebius H, et al. Swift heavy ion track formation in SrTiO<sub>3</sub> and TiO<sub>2</sub> under random, channeling and near-channeling conditions. *J Phys D: Appl Phys.* 2017;50:205302.
7. Liu N, Haublein V, Zhou XM, et al. "Black" TiO<sub>2</sub> nanotubes formed by high-energy proton implantation show noble-metal-catalyst free photocatalytic H<sub>2</sub>-evolution. *Nano Lett.* 2015;15:6815-6820.
8. Tsuji H, Sagimori T, Kurita K, Gotoh Y, Ishikawa J. Surface modification of TiO<sub>2</sub> (rutile) by metal negative ion implantation for improving catalytic properties. *Surf Coat Technol.* 2002;158:208-213.
9. Gunnlaugsson HP, Mantovan R, Masenda H, et al. Defect annealing in Mn/Fe-implanted TiO<sub>2</sub> (rutile). *J Phys D: Appl Phys.* 2014;47:065501.
10. Joshi SR, Padmanabhan B, Chanda A, Ojha S, Kanjilal D, Varma S. Complex damage distribution behaviour in cobalt implanted rutile TiO<sub>2</sub> (110) lattice. *Nucl Instrum Methods Phys Res, Sect B.* 2017;410:114-121.
11. Khubeis I, Fromknecht R, Meyer O. Lattice location and electrical conductivity in Sb-implanted rutile. *Phys Rev B: Condens Matter.* 1997;55:136-141.
12. Uberuaga BP, Bai XM. Defects in rutile and anatase polymorphs of TiO<sub>2</sub>: kinetics and thermodynamics near grain boundaries. *J Phys: Condens Matter.* 2011;23:435004.
13. Zheng SK, Wang TM, Wang C, Xiang G. Photocatalytic activity study of TiO<sub>2</sub> thin films with and without Fe ion implantation. *Nucl Instrum Methods Phys Res, Sect B.* 2002;187:479-484.
14. Zheng SK, Wang TM, Wang C, Xiang G. Improvement of photocatalytic activity of TiO<sub>2</sub> thin film by Sn ion implantation. *Vacuum.* 2001;65:155-159.
15. Shukur HA, Sato M, Nakamura I, Takano I. Characteristics and photocatalytic properties of thin film prepared by sputter deposition and post-n<sup>+</sup>ion implantation. *Adv Mater Sci Eng.* 2012;2012:1-7.
16. Shieh Y-N, Chang Y-Y. Influence of cobalt ion implantation on optical properties of titanium dioxide thin films. *Thin Solid Films.* 2010;518:7464-7467.
17. Robinson M, Marks NA, Whittle KR, Lumpkin GR. Systematic calculation of threshold displacement energies: case study in rutile. *Phys Rev B: Condens Matter.* 2012;85:104105. <https://doi.org/10.1103/physrevb.85.104105>.
18. Rath H, Dash P, Som T, et al. Structural evolution of TiO<sub>2</sub> nanocrystalline thin films by thermal annealing and swift heavy ion irradiation. *J Appl Phys.* 2009;105:074311.
19. Qin MJ, Kuo EY, Whittle KR, et al. Density and structural effects in the radiation tolerance of TiO<sub>2</sub> polymorphs. *J Phys: Condens Matter.* 2013;25:1-8. <https://doi.org/10.1088/0953-8984/25/35/355402>.
20. Qin L-Z, Liao B, Dong X-L, Wu X-Y, Hou X-G, Liu A-D. Ag/Fe:TiO<sub>2</sub> nano-catalysts prepared by Fe ion implantation and Ag nanoparticle deposition by electron beam irradiation. *Nucl Instrum Methods Phys Res, Sect B.* 2009;267:1077-1080.
21. Matsunami N, Uebayashi M, Hirooka K, Shimura T, Tazawa M. N ion irradiation enhancement of photocatalytic activity of TiO<sub>2</sub>. *Nucl Instrum Methods Phys Res, Sect B.* 2009;267:1654-1657.
22. Lumpkin GR, Smith KL, Blackford MG, et al. Experimental and atomistic modeling study of ion irradiation damage in thin crystals of the TiO<sub>2</sub> polymorphs. *Phys Rev B: Condens Matter.* 2008;77:214201.
23. Jensen J, Martin D, Surpi A, Kubart T. ERD analysis and modification of TiO<sub>2</sub> thin films with heavy ions. *Nucl Instrum Methods Phys Res, Sect B.* 2010;268:1893-1898.
24. Fernandes R, Patel N, Dholam R, Adami M, Miotello A. Low energy ion-beam modification of TiO<sub>2</sub> photocatalyst thin film for visible light absorption. *Surf Coat Technol.* 2009;203:2579-2583.
25. Jensen J, Sanz R, Martin D, et al. Implantation of anatase thin film with 100 keV 56 Fe ions: damage formation and magnetic behaviour. *Nucl Instrum Methods Phys Res, Sect B.* 2009;267:2725-2730.
26. Zhuo MJ, Uberuaga BP, Yan L, et al. Radiation damage at the coherent anatase TiO<sub>2</sub>/SrTiO<sub>3</sub> interface under Ne ion irradiation. *J Nucl Mater.* 2012;429:177-184.



27. Zhuo MJ, Fu EG, Yan L, et al. Interface-enhanced defect absorption between epitaxial anatase TiO<sub>2</sub> film and single crystal SrTiO<sub>3</sub>. *Scripta Mater.* 2011;65:807-810.
28. Zhang J, Lian J, Namavar F, et al. Nanosized rutile (TiO<sub>2</sub>) thin film upon ion irradiation and thermal annealing. *J Phys Chem C.* 2011;115:22755-22760.
29. Zhang J, Lian J, Namavar F, Ewing RC. Radiation response of nanocrystalline rutile TiO<sub>2</sub>. *Microsc Microanal.* 2009;15:1366-1367.
30. Li F, Lu P, Sickafus KE. Effects of Xe-ion irradiation at high temperature on single crystal rutile. *J Nucl Mater.* 2002;306:121-125.
31. Hazem R, Izerrouken M, Sari A, et al. Radiation damage induced by swift heavy ions in TiO<sub>2</sub> sol-gel films nanocrystallines. *Nucl Instrum Methods Phys Res, Sect B.* 2013;304:16-22.
32. Anderoglu O, Zhou MJ, Zhang J, et al. He<sup>+</sup> ion irradiation response of Fe-TiO<sub>2</sub> multilayers. *J Nucl Mater.* 2013;435:96-101.
33. Hartmann T, Wang LM, Weber WJ, et al. Ion beam radiation damage effects in rutile (TiO<sub>2</sub>). *Nucl Instrum Methods Phys Res, Sect B.* 1998;141:398-403.
34. Smith KA, Savva AI, Deng CJ, et al. Effects of proton irradiation on structural and electrochemical charge storage properties of TiO<sub>2</sub> nanotube electrodes for lithium-ion batteries. *J Mater Chem A.* 2017;5:11815-11824.
35. Atashbar MZS, Sun HT, Gong B, Wlodarski W, Lamb R. XPS study of Nb-doped oxygen sensing TiO<sub>2</sub> thin films prepared by sol-gel method. *Thin Solid Films.* 1998;326:238-244.
36. Baumard JF, Tani E. Electrical conductivity and charge compensation in nb doped TiO<sub>2</sub> rutile. *J Chem Phys.* 1977;67:857.
37. Yi T-F, Xie Y, Shu J, et al. Structure and electrochemical performance of niobium-substituted spinel lithium titanium oxide synthesized by solid-state method. *J Electrochem Soc.* 2011;158:A266.
38. Valentin CP, Pacchioni G, Selloni A. Reduced and n-type doped TiO nature of Ti species. *J Phys Chem C.* 2009;113:20543-20552.
39. Zhang SX, Kundaliya DC, Yu W, et al. Niobium doped TiO<sub>2</sub>: intrinsic transparent metallic anatase versus highly resistive rutile phase. *J Appl Phys.* 2007;102:013701.
40. Ruiz AMD, Dezanneau G, Arbiol J, Cornet A, Morante JR. Insights into the structural and chemical modifications of Nb additive on TiO<sub>2</sub> nanoparticles. *Chem Mater.* 2004;16:862-871.
41. Arbiol J, Cerdà J, Dezanneau G, et al. Effects of Nb doping on the TiO<sub>2</sub> anatase-to-rutile phase transition. *J Appl Phys.* 2002;92:853-861.
42. Morris DD, Dou Y, Rebane J, Mitchell CEJ, Egdell RG. Photoemission and STM study of the electronic structure of Nb-doped TiO<sub>2</sub>. *Phys Rev B: Condens Matter.* 2000;61:445-457.
43. Stoller RE, Toloczko MB, Was GS, Certain AG, Dwaraknath S, Garner FA. On the use of SRIM for computing radiation damage exposure. *Nucl Instrum Methods Phys Res, Sect B.* 2013;310:75-80.
44. Ziegler JF. The stopping and range of ions in matter (SRIM). *Nucl Instrum Methods Phys Res, Sect B.* 2013;268:1818-1823.
45. Giannuzzi LA, Stevie FA. Introduction to Focused Ion Beams: Instrumentation, Theory, Techniques, and Practice. New York, NY: In Springer; 2005.
46. Parish CM, Field KG, Certain AG, Wharry JP. Application of stem characterization for investigating radiation effects in BCC Fe-based alloys. *J Mater Res.* 2015;30:1275-1289.
47. Katiyar RS, Krishnan RS. The vibration spectrum of rutile. *Phys Lett A.* 1967;25:525-526.
48. Dayal B. The vibration spectrum of rutile. *Proc Indian Acad Sci.* 1950;32A:304-312.
49. Matossi F. The vibration spectrum of rutile. *J Chem Phys.* 1951;19:1543-1546.
50. McCreery RL. Raman Spectroscopy for Chemical Analysis. New York: John Wiley & Sons; 2000.
51. Swamy V, Muddle BC, Qing D. Size-dependent modifications of the raman spectrum of rutile TiO<sub>2</sub>. *Appl Phys Lett.* 2006;89:163118.
52. Porto SPS, Fleury PA, Damen TC. Raman spectra of TiO<sub>2</sub>, MgF<sub>2</sub>, ZnF<sub>2</sub>, FeF<sub>2</sub>, and MnF<sub>2</sub>. *Phys Rev.* 1967;154:522-526.
53. Frank O, Zukalova M, Laskova B, Kürti J, Koltai J, Kavan L. Raman spectra of titanium dioxide (anatase, rutile) with identified oxygen isotopes (16, 17, 18). *Phys Chem Chem Phys.* 2012;14:14567-14572.
54. Zhang J, Li MJ, Feng ZC, Chen J, Li C. UV Raman spectroscopic study on TiO<sub>2</sub>. I. Phase transformation at the surface and in the bulk. *J Phys Chem B.* 2006;110:927-935.
55. Balachandran U, Eror NG. Raman spectra of titanium dioxide. *J Solid State Chem.* 1982;42:276-282.
56. Zhou S, Potzger K, Krause M, et al. Origin of magnetic moments in defective TiO<sub>2</sub> single crystals. *Phys Rev B: Condens Matter.* 2009;79:113201.
57. Zhang Y, Harris CX, Wallenmeyer P, Murowchick J, Chen X. Asymmetric lattice vibrational characteristics of rutile TiO<sub>2</sub> as revealed by laser power dependent raman spectroscopy. *J Phys Chem C.* 2013;117:24015-24022.
58. Ishimaru M, Hirotsu Y, Li F, Sickafus KE. Surface morphology of ion-beam-irradiated rutile single crystals. *Appl Phys Lett.* 2000;77:4151.
59. Aoki Y, Yamamoto S, Takeshita H, Naramoto H. RBS/channeling analysis of damage and annealing processes of Nb-implanted TiO<sub>2</sub>. *Nucl Instrum Methods Phys Res, Sect B.* 1998;136:400-403.
60. Li F, Lu P, Ishimaru M, Sickafus K. Effect of heavy ion irradiation on near-surface microstructure in single crystals of rutile TiO<sub>2</sub>. *Philos Mag B.* 2000;80:1947-1954.
61. Li F, Ishimaru M, Lu P, Afanasyev-Charkin IV, Sickafus KE. Damage evolution in Xe-ion irradiated rutile (TiO<sub>2</sub>) single crystals. *Nucl Instrum Methods Phys Res, Sect B.* 2000;166-167:314-321.
62. Nomura K, Nakanishi T, Nagasawa Y, et al. Structural change induced in TiO<sub>2</sub> by swift heavy ions and its application to three-dimensional lithography. *Phys Rev B: Condens Matter.* 2003;68:064106. <https://doi.org/10.1103/PhysRevB.68.064106>.
63. Nomura K-I, Nakanishi T, Nagasawa Y, et al. Structure, structural phase transitions, mechanical properties, defects, etc. - structural change induced in TiO<sub>2</sub> by swift heavy ions and its application to three-dimensional lithography. *Phys Rev B: Condens Matter.* 2003;68:64106.
64. Bonfiglioli G, Ferro A, Mojoni A. Electron microscope investigation on the nature of tracks of fission products in mica. *J Appl Phys.* 1963;32:2499-2503.
65. Diebold U. The surface science of titanium dioxide. *Surf Sci Rep.* 2003;48:53-229.
66. Zhang YW, Xue HZ, Zarkadoula E, et al. Coupled electronic and atomic effects on defect evolution in silicon carbide under ion irradiation. *Curr Opin Solid State Mater Sci.* 2017;21:285-298.

67. Wolf GK. Modification of mechanical and chemical properties of thin films by ion bombardment. *Surf Coat Technol.* 1990;43:920-935.
68. Rauschenbach B, Gerlach JW. Texture development in titanium nitride films grown by low-energy ion assisted deposition. *Cryst Res Technol.* 2000;35:675-688.
69. Ma CH, Huang JH, Chen H. Texture evolution of transition-metal nitride thin films by ion beam assisted deposition. *Thin Solid Films.* 2004;446:184-193.
70. Holzapfel B, Betz V. Microstructure and texture evolution in oxide films prepared by ion-beam assisted laser deposition. *IEEE Trans Appl Supercond.* 1999;9:1479-1482.
71. Van Wyk GN, Smith HJ. Ion bombardment induced preferential orientation in polycrystalline Cu targets. *Radiat Eff Defects Solids.* 1978;38:245-247.
72. Van Wyk GN. The dependence of ion bombardment induced preferential orientation on the direction of the ion beam. *Radiat Eff Defects Solids.* 2011;57:45-50.
73. Carter G. Influence of thermal spikes on preferred grain orientation in ion-assisted deposition. *Phys Rev B.* 2000;62:8376-8390.
74. Van Wyk GN. The influence of ion species on ion bombardment induced preferential orientation. *Radiat Eff Defects Solids.* 2006;57:187-192.
75. Backman M, Djurabekova F, Pakarinen OH, et al. Atomistic simulations of meV ion irradiation of silica. *Nucl Instrum Methods Phys Res, Sect B.* 2013;303:129-132.
76. Backman M, Djurabekova F, Pakarinen OH, et al. Cooperative effect of electronic and nuclear stopping on ion irradiation damage in silica. *J Phys D: Appl Phys.* 2012;45:505305.
77. Toulemonde M, Dufour C, Meftah A, Paumier E. Transient thermal processes in heavy ion irradiation of crystalline inorganic insulators. *Nucl Instrum Methods Phys Res, Sect B.* 2000;166-167:903-912.
78. Toulemonde M, Dufour C, Paumier E. Transient thermal process after a high-energy heavy-ion irradiation of amorphous metals and semiconductors. *Phys Rev B: Condens Matter.* 1992;46:14362-14369.
79. Zarkadoula E, Xue H, Zhang Y, Weber WJ. Synergy of inelastic and elastic energy loss: temperature effects and electronic stopping power dependence. *Scripta Mater.* 2016;110:2-5.
80. Ridgway MC, Djurabekova F, Nordlund K. Ion-solid interactions at the extremes of electronic energy loss: examples for amorphous semiconductors and embedded nanostructures. *Curr Opin Solid State Mater Sci.* 2015;19:29-38.
81. Weber W, Oak Ridge National Laboratory. A coupled effect of nuclear and electronic energy loss on ion irradiation damage in lithium niobate. *Acta Mater.* 2016;105:429-437.
82. Weber WJ, Duffy DM, Thomé L, Zhang Y. The role of electronic energy loss in ion beam modification of materials. *Curr Opin Solid State Mater Sci.* 2015;19:1-11.

**How to cite this article:** Smith KA, Savva AI, Wu Y, et al. Effects of intermediate energy heavy-ion irradiation on the microstructure of rutile TiO<sub>2</sub> single crystal. *J Am Ceram Soc.* 2018;00:1–10.  
<https://doi.org/10.1111/jace.15576>